

Ionosphere-magnetosphere simulation of small-scale structure and dynamics

H. Zhu, A. Otto, D. Lummerzheim

Geophysical Institute, University of Alaska, Fairbanks

M. H. Rees¹ and B. S. Lanchester

Department of Physics, University of Southampton, Highfield, Southampton, England

Abstract. This work presents first results and the numerical methods of a highly improved two-dimensional three-fluid simulation model of the ionosphere-magnetosphere system. The model considers ionization and recombination, ion-neutral friction, the Hall term in Ohm's law, and various heat sources in the energy equations. The electrodynamic response and the evolution of the collision frequencies are treated self-consistently in the height-resolved ionosphere. This model is the first and to our knowledge the only simulation model that can resolve the dynamic and nonlinear electromagnetic interaction between the ionosphere and the magnetosphere. The simulation is aimed at modeling fast temporal and small spatial scale ionospheric structures associated, for instance, with filamentary aurora and ionospheric heating experiments. The results presented in this paper focus on ion and electron heating by different sources, i.e., ion heating due to plasma-neutral friction, electron heating resulting from energetic particle precipitation and by ohmic dissipation in strong field-aligned currents. This work is motivated by a specific auroral event that was observed simultaneously with optical and radar instruments. A consistent explanation of this event is possible in the presence of ohmic heating of electrons in a strong field-aligned electric current layer.

1. Introduction

The motivations for the present model are the electromagnetic effects of small-scale ionosphere-magnetosphere coupling, with emphasis on the ionospheric physics. There are ionospheric models which focus on the ionospheric transport and therefore are one-dimensional (i.e., they treat the altitude dependence of the relevant transport property) [e.g., Lummerzheim and Lilensten, 1994; Lanchester et al., 1997, 1998]. Others are large-scale ionospheric convection models [e.g., Roble and Rees, 1977; Sojka, 1989; Schunk, 1988; Roble et al., 1987; Maurits and Watkins, 1996] that determine convection by a steady state ion momentum equation. However, the neglect of the ion inertial term leaves out the physics of Alfvén wave propagation. The assumption of a steady state implies $\partial B/\partial t = 0$ and a potential electric field. While this assumption is reasonable for large-scale

lengths, it is violated on small-scale lengths. Our model does not have this limitation. Consequently, it is able to model, for instance, the formation of a field-aligned current layer through the propagation of Alfvén wave packets into the ionosphere. Such currents and Alfvén waves may be of central importance for filamentary aurora [e.g., Lanchester and Rees, 1987; Seyler, 1988, 1990; Otto and Birk, 1992, 1993; Haerendel, 1994; Lanchester et al., 1997; Stasiewicz and Potemra, 1998].

The present work introduces results of an improved two-dimensional three-fluid code. The original code [Birk and Otto, 1996, 1997] incorporated basic plasma transport coefficients such as ionization, plasma-neutral friction, resistivity, etc., but most of these parameters were kept constant in time. Values of these transport parameters were assumed such that the model yielded a reasonable ionospheric response to magnetospheric input such as the reflection of Alfvén waves, but the result of the simulation was unable to

¹ also at Geophysical Institute, University of Alaska, Fairbanks

describe properly the corresponding ionospheric modifications, similar to the model by *Dreher* [1997]. The improvements which are detailed in section 2 address a realistic altitude profile of ionization rates, electron and ion cooling rates, etc., and the modification in the plasma parameters (density and electron and ion temperatures) is fed back into the transport parameters. Thus the model includes the nonlinear two-dimensional (2-D) ionospheric dynamics. In this paper we will present a number of examples of such nonlinear effects.

Electron inertia is not included in our model for the present work because the length-scale of the electron inertia term is about 20 m, much smaller than the typical horizontal length-scale in our simulation (1 km). The electron inertia term is much smaller than other terms in Ohm's law.

Small-scale filamentary structure is very frequent in the auroral ionosphere [e.g., *Borovsky*, 1993; *Lanchester et al.*, 1994, 1997]. This is a strong indication for time-dependent processes which require ion inertia. In order to address the physics adequately it is also necessary to incorporate realistic ionospheric transport. However, there are always limitations to the degree that this is possible. For instance, to avoid including a complex electron transport code, the ionization rates in our model are parameterized by a characteristic energy and energy flux and then computed for an equilibrium neutral atmosphere with a prescribed temperature distribution. For the ionization rates (and electron cooling rates) it is important to identify the neutral species. These are obtained from a height profile of an average neutral molecular mass, since the neutrals are modeled as one fluid. The code can accommodate an altitude-varying ion mass. However, the present results are obtained for a fixed ion mass, O^+ . A variable ion composition would require expansion of the three-fluid to a multifluid code. Therefore effects which are specific to the presence and dynamics of more than one distinct ion species are not addressed. Extensions to multiple ion species and anisotropic pressures can be incorporated as the physical problems require such effects.

Here the simulation results are motivated by optical and radar (European incoherent scatter (EISCAT)) observations of small-scale discrete aurora. These observations and results from transport simulations are presented in a companion paper by *Lanchester et al.* [this issue] hereinafter referred to as L99. The one-dimensional transport simulations treat the ion chemistry, electron transport, and variations of the precipitating flux more accurately than is possible in the two-dimensional approach. Thus this work complements our results on the electrodynamics and spatial structure. The event discussed by L99 displays an unusual evolution of plasma number density, ion temperature, and electron temperature. Motivated by this, the simulation results in the

present paper focus on the formation of field-aligned current (FAC) layers, the associated heating of ions by the plasma motion in the Alfvén waves, and electron heating by precipitation and in particular by ohmic dissipation in the FAC. Other aspects of the two-dimensional dynamics such as nonlinear effects for FACs, electron densities, and conductivities will be the topic of a separate paper.

It is important to note that small spatial scales of the order of kilometers necessitate a time-dependent model. The usually fast motion of discrete aurora (km s^{-1}) implies that plasma is exposed to the effects of thin current layers and precipitation for only a few seconds typically. Note that a thin current layer associated with discrete aurora is not frozen to the ionospheric convection [*Wescott et al.*, 1975; *Haerendel et al.*, 1993; *Lanchester et al.*, 1997]. Typical relaxation times (for instance, to achieve a steady electron temperature) range from a fraction of a second in the lower E region to several seconds in the F region. Also, the time for an Alfvén wave to travel through the F and E regions is of the order of a second.

In the next section we introduce the equations and the initial and boundary conditions of the two-dimensional three-fluid model. The model results are presented in section 3, and a summary and conclusions are given in the final section.

2. Numerical Model

2.1. Basic Equations

In this study we use a full set of three-fluid equations (electrons, ions, and neutrals) [e.g., *Birk and Otto*, 1996]. The normalized equations are given by

$$\frac{\partial \rho}{\partial t} = -\nabla \cdot \rho \mathbf{v} + \iota \rho - \beta \rho^2 \quad (1)$$

$$\frac{\partial \rho_n}{\partial t} = -\nabla \cdot \rho_n \mathbf{v}_n - \iota \rho + \beta \rho^2 \quad (2)$$

$$\begin{aligned} \frac{\partial \rho \mathbf{v}}{\partial t} = & -\nabla \cdot (\rho \mathbf{v} \mathbf{v}) - \frac{1}{2} \nabla p + \rho \mathbf{g} \\ & + (\nabla \times \mathbf{B}) \times \mathbf{B} + \rho \mathbf{v} (\iota - \beta \rho) \\ & - \rho \nu_{in} (\mathbf{v} - \mathbf{v}_n) \end{aligned} \quad (3)$$

$$\begin{aligned} \frac{\partial \rho_n \mathbf{v}_n}{\partial t} = & -\nabla \cdot (\rho_n \mathbf{v}_n \mathbf{v}_n) - \frac{1}{2} \nabla p_n + \rho_n \mathbf{g} \\ & - \rho \mathbf{v}_n (\iota - \beta \rho) - \rho \nu_{in} (\mathbf{v}_n - \mathbf{v}) \end{aligned} \quad (4)$$

$$\begin{aligned} \frac{\partial \mathbf{B}}{\partial t} = & \nabla \times \left(\frac{1}{ne} \nabla p_e \right) + \nabla \times (\mathbf{v} \times \mathbf{B}) \\ & - \nabla \times \left(\frac{1}{ne} (\nabla \times \mathbf{B}) \times \mathbf{B} \right) \\ & - \nabla \times (\eta \nabla \times \mathbf{B}) \end{aligned} \quad (5)$$

$$\begin{aligned}
\frac{\partial p}{\partial t} = & -\mathbf{v} \cdot \nabla p - \gamma p \nabla \cdot \mathbf{v} + (\iota - \beta \rho) T_n \\
& + (\gamma - 1) \left(2\eta (\nabla \times \mathbf{B})^2 \right. \\
& + \iota e_c - 3 \frac{\nu_{in} \rho}{m_i + m_n} (T_i - T_n) \\
& \left. + \left(\frac{m_n \nu_{in} \rho}{m_i + m_n} + \iota m_i \right) (v - v_n)^2 \right) \\
& + 3\nu_{eff} \rho (T_n - T_e) + \frac{\partial}{\partial z} \left(\lambda_e \frac{\partial T_e}{\partial z} \right) \quad (6)
\end{aligned}$$

$$\begin{aligned}
\frac{\partial T_e^\kappa}{\partial t} = & -\nabla \cdot (T_e^\kappa \mathbf{v}_e) \\
& + T_e^{\kappa-1} \left(3\nu_{ei} (T_i - T_e) \right. \\
& + 3\nu_{eff} (T_n - T_e) + \frac{2\eta}{n} (\nabla \times \mathbf{B})^2 \\
& + \frac{\iota e_c}{n} - \frac{\iota T_e}{(\gamma - 1)n} \\
& \left. + \frac{1}{n} \frac{\partial}{\partial z} \left(\lambda_e \frac{\partial T_e}{\partial z} \right) \right) \quad (7)
\end{aligned}$$

$$\begin{aligned}
\frac{\partial p_n}{\partial t} = & -\mathbf{v}_n \cdot \nabla p_n - \gamma_n p_n \nabla \cdot \mathbf{v}_n - (\iota - \beta \rho) k T_n \\
& + (\gamma_n - 1) \left(3 \frac{\nu_{ni} \rho_n}{m_i + m_n} (T_i - T_n) \right. \\
& \left. - \iota \rho T_n + \frac{m_i \rho_n \nu_{in}}{m_i + m_n} (v_n - v)^2 \right) \\
& + 3\nu_{eff} \rho (T_e - T_n) \quad (8)
\end{aligned}$$

where ρ and ρ_n are the total plasma and neutral mass density; m_i and m_n are the ion and neutral particle mass; T_e , T_i , and T_n are the electron, ion, and neutral temperatures; p , p_e , and p_n are the total plasma pressure, electron pressure, and neutral pressure; n is the plasma number density; \mathbf{v} , \mathbf{v}_e , and \mathbf{v}_n are plasma, electron, and neutral velocities; \mathbf{B} is the magnetic induction vector; \mathbf{g} is the gravitational acceleration; ι is the ionization rate; ν_{in} is the ion-neutral, ν_{ei} is the Coulomb, and ν_{eff} is the effective collision frequency between electrons and neutrals; η is the resistivity; γ and γ_n are the ratios of specific heats for the plasma and neutrals; e_c is the average energy that goes into electron heating for each ionization process (a typical value is 2 eV); λ_e is the electron heat conduction coefficient; and $\kappa = 1/(\gamma - 1)$. Energy conservation requires $\gamma_n = \gamma = 5/3$.

The ionization rate ι , the recombination frequency β , and the electron heating rate associated with ionization e_c are parameterized by using input from an ionospheric transport computation [Lummerzheim, 1992]. The electron heat conduction coefficient λ_e and the effective electron-neutral collision frequency ν_{eff} are from the National Center for Atmo-

spheric Research (NCAR) thermosphere ionosphere mesosphere electrodynamics general circulation model (TIME-GCM) [Roble, 1996]. The resistivity in the simulation is given by

$$\eta = \eta_{ei} + \eta_{en} + \eta_{in}, \quad (9)$$

with

$$\eta_{ei} = \lambda \nu_{ei} \tau_A$$

$$\eta_{en} = \lambda \nu_{en} \tau_A$$

$$\eta_{in} = \lambda \nu_{in} \tau_A$$

where ν_{ei} , ν_{en} , and ν_{in} are the electron-ion, electron-neutral, and ion-neutral collision frequencies; $\tau_A = l_0/v_A$ is Alfvén time; and $\lambda = (c/(\omega_{pe} l_0))^2$ is a normalization coefficient. The parameterization of collision frequencies ν_{ei} , ν_{en} , and ν_{in} is given by Schunk [1983].

In the computation we assume singly charged ions, charge neutrality, and the following definitions:

$$n = n_e = n_i$$

$$\rho = n(m_e + m_i)$$

$$p = p_e + p_i$$

$$\rho \mathbf{v} = \rho_e \mathbf{v}_e + \rho_i \mathbf{v}_i.$$

The results are presented in physical units. In the simulation, all the quantities in (1) through (8) are normalized to characteristic values of the system, i.e., the horizontal length scale to the typical length $l_0 = 1.0$ km; the vertical length scale to $l_{z0} = 500$ km; plasma and neutral number density n and n_n to $n_0 = 50,000 \text{ cm}^{-3}$; mass m_e , m_i , and m_n to the oxygen mass $m_0 = m_{O^+}$; mass density ρ and ρ_n to $\rho_0 = n_0 m_0$; magnetic field B to $B_0 = 0.5$ G; vertical velocity v_z , v_{ez} , and v_{nz} to the Alfvén velocity $v_A = B_0(\mu_0 \rho_0)^{-1/2}$ (1220 km s^{-1}); horizontal velocity \mathbf{v}_x and \mathbf{v}_y to $l_0/l_{z0} v_A$ (2.44 km s^{-1}); pressure p , p_e , and p_n to $P_0 = B_0^2/(2\mu_0)$; T_e and T_n to $T_0 = P_0/(n_0 k)$ (k is the Boltzmann constant); and time t to characteristic Alfvén transit time $\tau_A = l_{z0}/v_A$.

We use Cartesian coordinates in the simulation with x and y (invariant) perpendicular to the magnetic field; z is along the unperturbed magnetic field, which in the Northern Hemisphere is in the negative z direction.

The equations are solved with a modified leapfrog scheme [Potter, 1973; Birn, 1980] of second-order accuracy in space and time. The grid points in the horizontal (x direction) are uniformly separated. In the vertical direction a nonuniform grid is used with the best resolution of 4 km at the bottom boundary of the simulation box.

2.2. Equilibrium and Initial Perturbation

The simulation region extends from 100 km (lower E region) to 1100 km altitude with the main magnetic field in

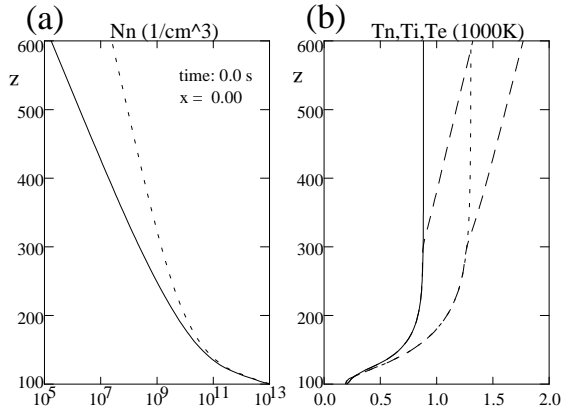


Figure 1. (a) Altitude neutral density profile for solar minimum conditions (solid line) and solar maximum conditions (dotted line) conditions and (b) temperature profiles for the neutral atmosphere (solid line for solar minimum, dashed and dotted lines for solar maximum), for ions (initially identical to the neutrals), and for electrons (short dashes branching off the neutral temperature).

the vertical direction. The neutral fluid is initially in hydrostatic equilibrium with a temperature T_n and density n_n chosen for solar minimum and solar maximum conditions from the Mass Spectrometer Incoherent Scatter (MSIS) model [Hedin, 1991; Rees, 1989] (see Figure 1). The neutral number density and temperature profiles are significantly different at high altitudes for solar minimum and solar maximum conditions. These differences yield ion heating at different altitudes. The neutral number density n_n in the simulation is the sum of three species, i.e., n_{N_2} , n_O , and n_{O_2} ; all contribute to ionization and electron cooling.

We assume that the ions initially have the same temperature profile as the neutrals. The electron temperature equals the neutral only at the lower boundary of the system but gradually increases (above 250 km) with altitude to a value of about 1300 K for solar minimum conditions and 1750 K for the solar maximum case at the 600 km. To determine the initial plasma density profile, we assume a high-altitude number density of $5 \times 10^4 \text{ cm}^{-3}$. Using force equilibrium and the $T_e + T_i$ profile, we obtain the ion density profile. This profile is adjusted at lower altitudes to a typical density measured by the EISCAT radar during the event being analyzed. A small resulting force imbalance at low altitudes is negligible because the plasma is strongly collision dominated and corresponding effects occur on much longer timescales than considered here.

An initial perturbation of the plasma velocity and the hor-

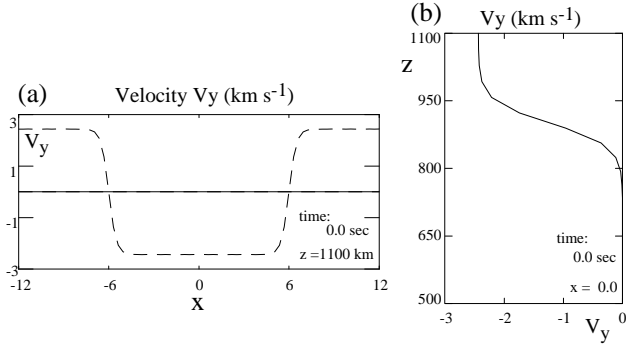


Figure 2. Initial velocity perturbation associated with the Alfvén waves in a horizontal cut (a) at the top boundary and (b) in a vertical cut at $x = 0$.

izontal magnetic field is applied at the top boundary with

$$v_y = \frac{v_{y0}}{2} (1 + \tanh(0.015(z - 800))) \tanh(2.0(x + 6.0)) \quad (10)$$

for $x < 0$ and

$$v_y = -\frac{v_{y0}}{2} (1 + \tanh(0.015(z - 800))) \tanh(2.0(x - 6.0)) \quad (11)$$

for $x \geq 0$, and the magnetic field perturbation is given by

$$B_y = -v_y(\mu_0 \rho)^{1/2}. \quad (12)$$

Note that the perturbation defined in (10), (11), and (12) contributes to the initial conditions and must be consistent with the boundary conditions.

This initial perturbation propagates into the ionosphere as a pair of Alfvén waves which produce two field-aligned current layers at $x = -6$ km (upward) and $x = 6$ km (downward). The amplitude is $v_{y0} = 1.0$, which corresponds to 2.44 km s^{-1} . The velocity profile of the initial perturbation is shown in Figure 2a as a function of x , and the plot in Figure 2b illustrates the altitude profile of the amplitude. The magnetospheric boundary condition is chosen such that the wave train maintains its amplitude. The structure of the Alfvén wave and the pair of FACs is presented in the upper plot of Figure 3a. The field-aligned current is closed by polarization currents at the leading edge of the wave trains. Note that the separation of the the upward and downward current layers is chosen arbitrarily. We are interested in the properties of the upward current layer mostly. The choice of two current layers allows simple periodic boundary conditions along x and shows nicely the closure of the field-aligned current by Pedersen currents (at later times).

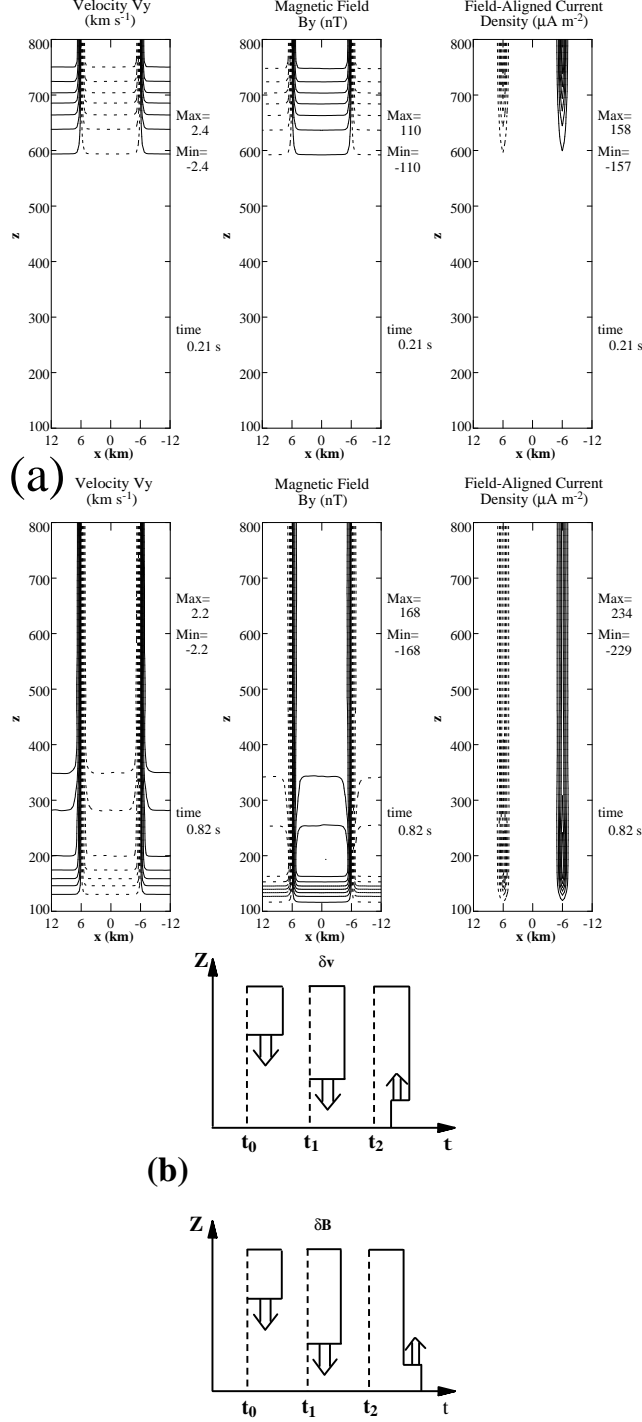


Figure 3. (a) Two-dimensional contour plots for the velocity V_y , the magnetic field B_y , and the field-aligned current density j_y at time $t = 0.21$ s and at $t = 0.82$ s. (b) The sketch in illustrates the velocity and magnetic field perturbations for the incoming Alfvén wave (t_0 and t_1) and shortly after the reflection (t_2).

For the present topic the precise magnetospheric cause for the field-aligned currents is not relevant. However, we note that sheared plasma motion, which is typical for magnetospheric boundary layers, can be such a cause.

2.3. Boundary Conditions

In the simulation we use a periodic boundary condition in the x direction, which allows waves to propagate freely through the system. At the lower boundary of the simulation box ($z = 100$ km), the densities ρ , ρ_n , pressures p , p_e , p_n , and temperatures T_e and T_n , are given by continuous boundary conditions; that is, the boundary values of these quantities are computed by extrapolation. For the magnetic field \mathbf{B} , current \mathbf{j} , and plasma velocity \mathbf{v} , however, we determine the boundary values using Ohm's law.

After obtaining the boundary values for ρ and p , we compute the collision frequencies ν_{en} , ν_{in} , and ν_{ei} and the Pedersen and Hall conductivities. We extrapolate the electric field from the physical boundary to a mathematical boundary and use Pedersen and Hall conductivities to compute the current density from $\mathbf{j} = \sigma \cdot \mathbf{E}$ on this boundary. Similarly, the boundary value for the plasma velocity \mathbf{v} is determined by

$$\mathbf{v}_i = \frac{e}{m_i} \left(\frac{\nu_{in}}{\omega_{ci}^2 + \nu_{in}^2} \mathbf{E}_\perp + \frac{\omega_{ci}}{\omega_{ci}^2 + \nu_{in}^2} \mathbf{E} \times \hat{\mathbf{b}} \right), \quad (13)$$

where ω_{ci} is the ion gyrofrequency and $\hat{\mathbf{b}}$ is the unit vector of unperturbed magnetic field. Finally, the magnetic field \mathbf{B} is determined from the relation $\mathbf{j} = \nabla \times \mathbf{B}$.

At the top boundary of the system ($z = 1100$ km) we use free boundary conditions for most quantities; that is, we calculate the value at the boundary from its value inside the physical boundary of the system by extrapolation. This maintains the initial perturbation for the Alfvén waves and allows the transmission of the waves which are reflected in the lower ionosphere.

Finally, we note that the chosen model represents the formation of a stagnant current layer rather than a drifting one. We have chosen this configuration because it illustrates basic properties of a field-aligned current layer. The precise properties of a moving current layer depend on the speed relative to the background ionospheric plasma. For instance, the duration for which the electrons are exposed to ohmic heating in the current depends on the width, magnitude, and drift velocity of the current.

3. Results: Ion and Electron Heating in the Ionosphere

Various terms in (6) and (7) can increase the ion or electron temperature in the ionosphere. In the electron temper-

ature equation (7), two source terms can heat electrons, i.e., the ohmic heating term $\eta j^2/(\rho nk)$ ($\mathbf{j} = \nabla \times \mathbf{B}$) and the heating term from energetic particle precipitation $\epsilon_c/(nk)$. Thermal energy loss terms are due to thermal contact between electron and other particles, for example, cooling due to electron-neutral collisions $\nu_{\text{eff}}(T_n - T_e)$ (rotational, vibrational, electronic excitations [Roble, 1996]) and cooling by ions $\nu_{ei}(T_i - T_e)$. The total pressure equation includes also the frictional (Joule) heating term $(\rho m_n \nu_{in} \rho / (m_i + m_n) + m_i l)(v - v_n)^2$ in addition to ohmic heating and particle precipitation. Ions and neutrals are heated by this process. Further, advection and heat conduction can alter the local temperature. Before we discuss our results, it seems helpful to give a brief illustration of the propagation of Alfvén waves in the ionosphere-magnetosphere system.

3.1. Alfvén Wave Propagation and Reflection

The initial perturbation launches a pair of Alfvén waves carrying the velocity and magnetic field perturbation along the magnetic field. The pair of Alfvén waves is separated by upward and downward field-aligned currents. The waves travel with a speed of about 1000 km s^{-1} . In the lower ionosphere the waves are reflected in the region of enhanced Pedersen conductivity (i.e., larger collision frequency and friction) [e.g., Hughes and Southwood, 1976]. The reflection coefficient is given by Maltsev *et al.* [1977]. The top plot of Figure 3a show the wave perturbations for v_y and B_y and the associated field-aligned current shortly after the start of the simulation. The lower plot in Figure 3a show the wave perturbations and the field-aligned current density shortly after the leading edge of the wave is reflected. The velocity of the reflected wave decreases, while the magnetic field perturbation increases. The magnetic field perturbation and the field-aligned current density are about 50% larger at 200 km, indicating a reflection coefficient of roughly 50%. The major portion of the field-aligned current is closed through a Pedersen current in the E region. A smaller polarization current is associated with the leading edge of the reflected wave.

A decrease in the plasma convection is caused by the upward wave vector of the reflected wave. Figure 3b shows a schematic of the wave propagation and reflection in terms of the magnetic field and velocity perturbation. This work considers only the case of very long wavelengths corresponding to frequencies larger than about 10 s. Ions are heated by the plasma-neutral friction in the convection which is switched on and modulated by the Alfvén waves and in the Pedersen current regions. A particular source for electron heating associated with this configuration is the ohmic heating in the field-aligned current regions.

3.2. Ion Heating by Friction Between Ions and Neutrals

We examined the ion heating by the frictional force between ions and neutrals for solar minimum and solar maximum conditions (Figure 1) with neutral temperature profiles from the MSIS model [Hedin, 1991; Rees, 1989].

The simulation uses the initial perturbation given by (10), (11), and (12). Ion heating occurs, for instance, in the region between the two field-aligned current layers, i.e. around $x = 0$, where the ions are driven by the Alfvén wave. Plate 1 shows the ion temperature increase by frictional heating as a function of time for solar minimum and solar maximum conditions. The magnitude of the temperature increase and the height profiles are very different for the two cases, due primarily to the ionospheric conditions responsible for the reflection of the Alfvén waves.

The simulation shown in Plate 1 was started with a symmetric perturbation and no initial Pedersen current. The presence of an initially asymmetric Pedersen current would yield asymmetric heating across the current layers, as observed by L99, and Opgenoorth *et al.* [1990].

The ion heating $(m_n \nu_{in} \rho / (m_i + m_n) + m_i l)(v - v_n)^2$ in the total plasma energy (pressure) equation (6) is proportional to the collision frequency and to the square of the ion velocity (we assume $\mathbf{v}_n = 0$) when there is no particle precipitation. The collision frequency between ions and neutrals increases exponentially with decreasing height, thereby heating significantly the ions as the Alfvén wave propagates into the E region of the ionosphere. Heating increases with decreasing height until the wave is reflected [Hughes and Southwood, 1976]. The reflected wave decreases the ion velocity with a corresponding decrease of the ion heating rate. Thermal contact between ions and neutrals cools the ions efficiently at low altitudes. As shown in Plate 1, the ion temperature initially reaches a maximum at low altitude. After reflection of the Alfvén wave, the maximum shifts to higher altitude. A deceleration of the convection velocity due to friction contributes to the decrease of ion heating.

3.3. Electron Heating by Particle Precipitation

The simulation results of Alfvén wave propagation show that ions are strongly heated in the region outside the field-aligned current sheets. The electron temperature remains mostly unchanged during the process of increasing ion temperature. There are two source terms in the electron temperature equation (7), i.e., ohmic heating $\eta j^2/(\rho nk)$ in a field-aligned current layer and heating from ionization $\epsilon_c/(nk)$.

Before we discuss the results of electron heating by ionization, we first illustrate some basic physics. In the electron temperature equation (7), we only consider the ionization

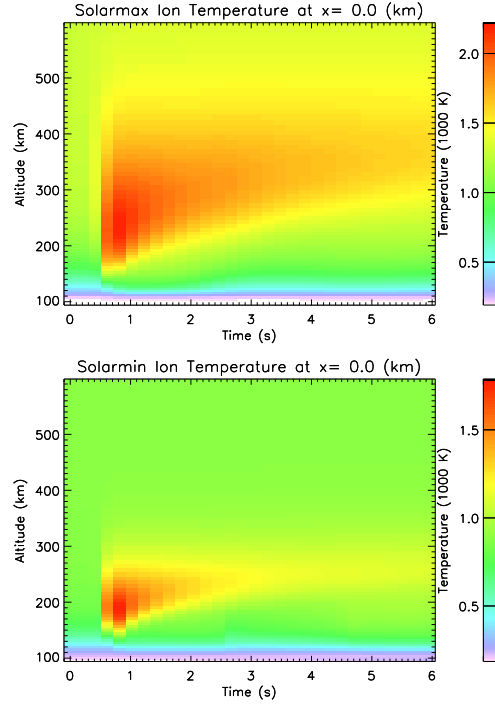


Plate 1. Altitude versus time plots of the ion temperature for (top) solar maximum conditions and (bottom) solar minimum conditions.

source:

$$\frac{\partial T_e^\kappa}{\partial t} = \frac{\iota e_c}{nk} T_e^{\kappa-1} - \frac{\iota}{(\gamma-1)n} T_e^\kappa. \quad (14)$$

Defining $T_c = (\gamma - 1)e_c/k$, (14) can be rewritten

$$\frac{\partial T_e}{\partial t} = \frac{\iota}{n}(T_c - T_e). \quad (15)$$

For a typical value of $e_c = 2$ eV, we obtain $T_c = 1.55 \times 10^4$ K, which is much higher than the usual electron temperature in the ionosphere. Equation (15) shows that electron heating by ionization is proportional to the ionization rate and inversely proportional to the plasma number density. Electron heating by ionization is fast when the electron temperature is low, i.e., at the beginning of ionization. As the electron temperature increases, the heating rate by ionization slows down.

In our simulation the ionization rate is parameterized from the output of a 1-D transport code [Lummerzheim, 1992]. The input to the transport calculation is an energy flux of 40 mW m^{-2} with a characteristic energy E_{char} of 1.0 keV in a Maxwellian spectrum. The resulting height profile is shown in Figure 4. The ionization peak is at about 130 km. The result of the simulation, adopting the ionization profile of Figure 4 for solar minimum conditions, is shown in the

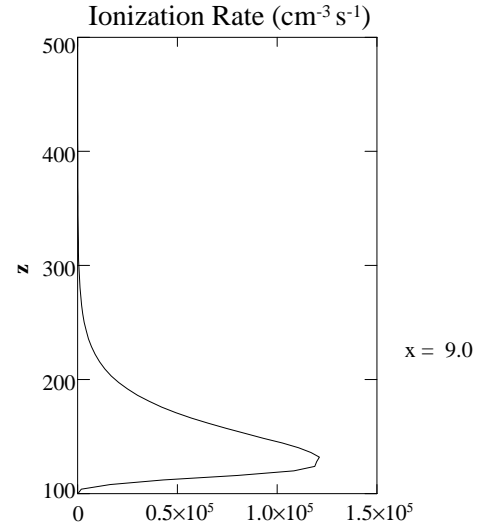


Figure 4. Height profile for the ionization rate for the solar minimum case and an incident Maxwellian energy flux of 40 mW m^{-2} with a characteristic energy E_{char} of 1.0 keV.

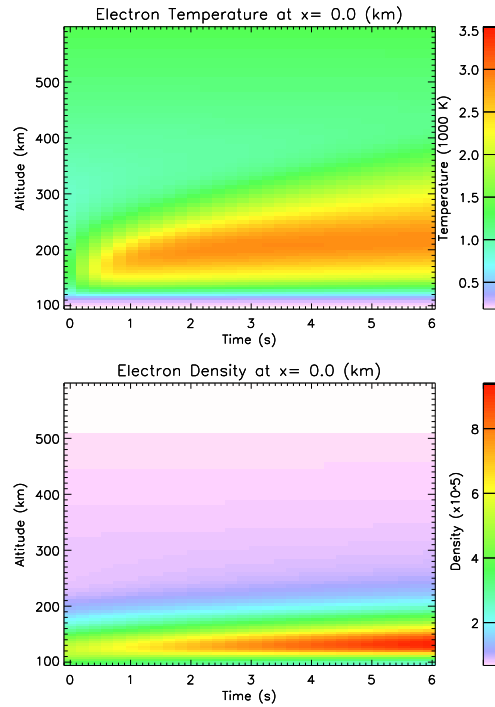


Plate 2. (top) Electron temperature evolution for the ionization shown in Figure 4 and (bottom) number density.

top panel of Plate 2. The ionization was applied only in a limited vicinity around $x = 0$.

The evolution of the electron temperature profile follows the physical arguments implied by (15). At early times the maximum electron temperature increase is at about 170 km, slightly higher than the altitude of maximum ionization rate. The initial number density increases with decreasing altitude (down to about 130 km, bottom panel of Plate 2). Thus the initial energy deposition per electron has a maximum slightly above the region of maximum density. As time proceeds, the plasma number density at lower altitude increases faster due to ionization, such that energy deposition per electron decreases further. In addition, the cooling term $\nu_{\text{eff}}(T_e - T_n)$ in the electron temperature equation is large at lower altitudes. The combined effect shifts the maximum electron temperature to higher altitude. Heat conduction contributes to this shift, as will be illustrated later.

The ion temperature change is very similar that shown in Plate 1 (solar minimum). The only difference is that the ionization changes the density profile and reflection properties for the Alfvén wave, which, however, does not change the heating profile significantly.

3.4. Electron Heating by Ohmic Dissipation

A strong field-aligned current heats the electrons by ohmic dissipation. The heating rate is given by ηj^2 , where η is the resistivity and \mathbf{j} is the current density.

The initial plasma flow and the sheared magnetic field generate two field-aligned current layers, with the upward current layer at $x = -6$ km and the downward current layer at $x = 6$ km. As the perturbation propagates with the Alfvén wave into the ionosphere, the two field-aligned current layers expand over the entire simulation box (Figure 3a). Reflection of the Alfvén wave increases the amplitude of the magnetic field perturbation, resulting in an increase of the current density with time as the current sheets develop. In Figure 3a we show that at $t = 0.82$ s, just after the wave is reflected, the magnetic field perturbation is enhanced from 110 nT (at $t = 0.21$ s) to 170 nT, and the field-aligned current is increased to about $230 \mu\text{A m}^{-2}$. Such values are large but not unreasonable for filamentary aurora [e.g., *Lanchester et al.*, 1997; *Stasiewicz and Potemra*, 1998; *Stasiewicz et al.*, 1998].

Figure 5a shows details of the field-aligned current structure, the velocity perturbation (v_y), the magnetic field perturbation (b_y), and the field-aligned current (j_z) at $t = 4$ s. Figure 5b shows the vector plot of the field-aligned current and the electron velocity as well as the ion velocity. Note

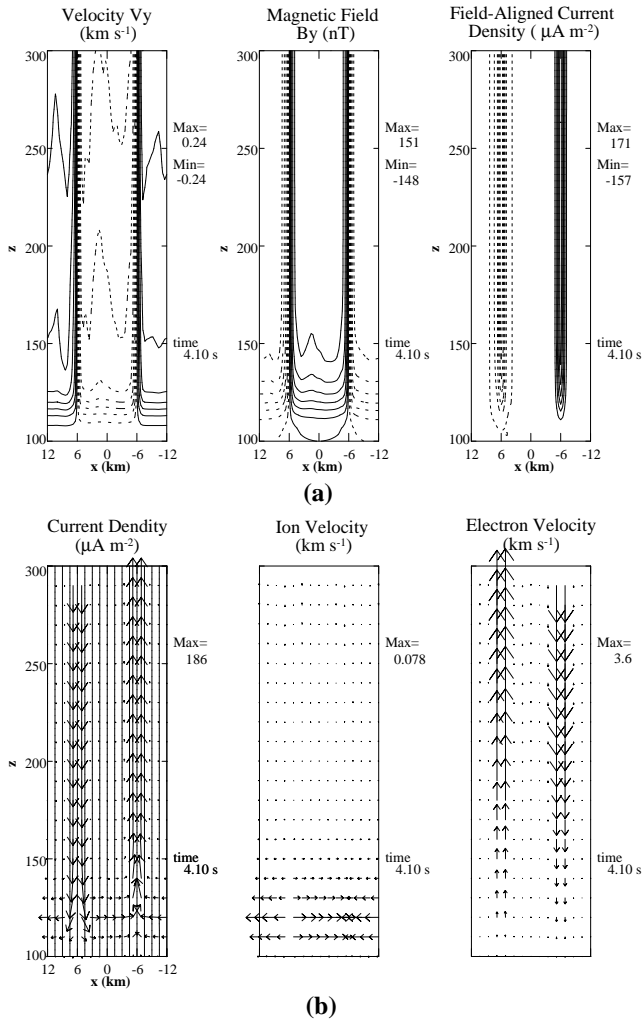


Figure 5. (a) Two-dimensional contour plots of velocity V_y , magnetic field B_y , field-aligned current density j_y and (b) vector plots of current density, ion velocity, and electron velocity for the solar minimum case without precipitation.

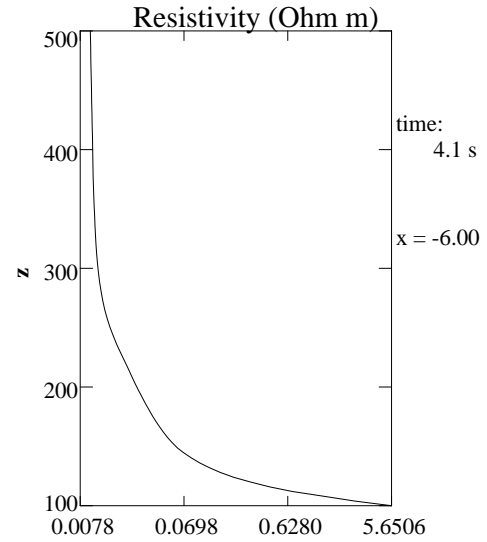


Figure 6. Parallel resistivity in the upward current layer ($x = -6$ km) at time $t = 4.1$ s.

that both upward and downward field-aligned currents are carried by electrons, while the closing Pedersen current at about 117 km is carried by ions.

We examine electron heating by ohmic dissipation at the center of the upward current layer. Figure 6 shows a plot of the parallel resistivity at the center of the upward current layer. The resistivity decreases exponentially with altitude. Since the current density is almost constant with altitude, the ohmic heating rate should be maximum at the lower end of the field-aligned current layer and decrease exponentially with the altitude. Electron cooling by collisions with neutrals and ions increases with decreasing altitude. Therefore the change of electron temperature is the result of both heating and cooling.

Plate 3 shows the electron temperature evolution at the center of the upward field-aligned current. The electron temperature changes are due to the combined effect of ohmic heating and collisional cooling. As the field-aligned current propagates into the ionosphere, the electrons at higher altitude are heated first. The heat source moves down to lower altitudes with the Alfvén wave. It takes only about 0.6 s for the Alfvén wave to arrive at the lower boundary. After about 2 s, the balance between heating and cooling yields a maximum electron temperature at about 200 km. The lower boundary of the large electron temperature increase appears as low as 170 km. Note that ohmic dissipation has a negligible effect on ion heating.

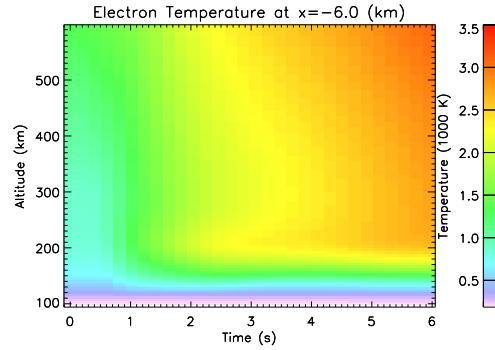


Plate 3. Electron temperature evolution for the solar minimum case in the upward current layer at $x = -6$ km.

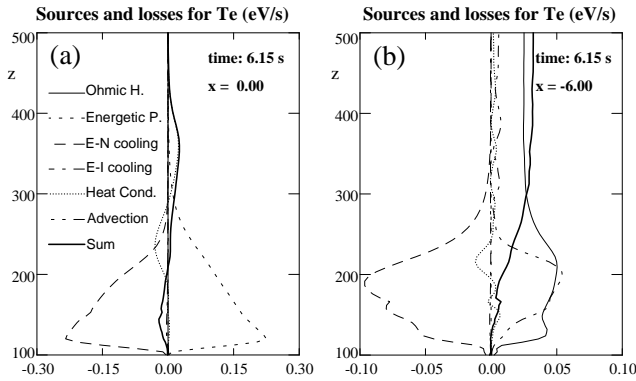


Figure 7. Plot of source and loss terms for the electron temperature for (a) the precipitation case (a) shown in Plate 2 and (b) the ohmic heating case shown in Plate 3.

3.5. Sources and Losses for the Electron Temperature

Figures 7a and 7b illustrate the contributions of various source and loss terms to the evolution of the electron temperature in eV s^{-1} per particle for the cases of precipitation (Figure 7a) and ohmic heating in the upward FAC region (Figure 7b). The bold solid lines in the plots represent the sum of all source and loss terms.

For the case of precipitation, electron heating in the upper ionosphere is due to heat conduction. In the lower portion of the ionosphere the electron temperature is close to a steady state where the heating by particle precipitation and losses due to electron-neutral interaction and heat conduction balance each other. There is a small negative residual in the overall temperature evolution at lower altitudes. This is caused by the increasing number of electrons due to the precipitation such that the heating per particle from the precipitation is slowly decreasing in time. The temperature maximum at this time is at about 220 km altitude. Neutral

collisions become rare at this altitude such that the dominant transport is heat conduction.

In the case of ohmic heating (Figure 7b) the lower portion of the electron temperature is also close to a steady state. However, different from the precipitation case, the upper part of the current layer (above 250 km) is still heated. Since the upper temperature profile shows a very small gradient, heat conduction is less important than in the precipitation case. The dominant source for energy input is the ohmic heating. A significant additional source for energy deposition or transport is advection in the region with a large gradient in the electron temperature. Note that the field-aligned current implies an electron drift of about 4 km s^{-1} . The transport by convection provides a positive contribution in the upward current layer and (without illustration) a negative one in the downward current layer (because cold material is carried upward). In the lower portion of the ionosphere the positive source terms are efficiently compensated by electron-neutral collisions.

Since the electron-neutral collision frequency is exponentially increasing with decreasing altitude, the characteristic timescale to achieve a steady state decreases with altitude. This leads to an evolution where a steady electron temperature is assumed faster in the lower ionosphere.

4. Comparison With Radar Observation

The EISCAT radar and optical observations (January 28, 1995) are presented and discussed in detail by L99. The event was characterized by the presence of filamentary aurora in the field of view of the radar and imagers.

As shown in Figure 1 of L99, there occurred an initial increase of the ion temperature in a region of decreasing electron density and temperature. During the subsequent decrease in ion temperature the electron temperature suddenly increased. The increase in T_e occurred without a cor-

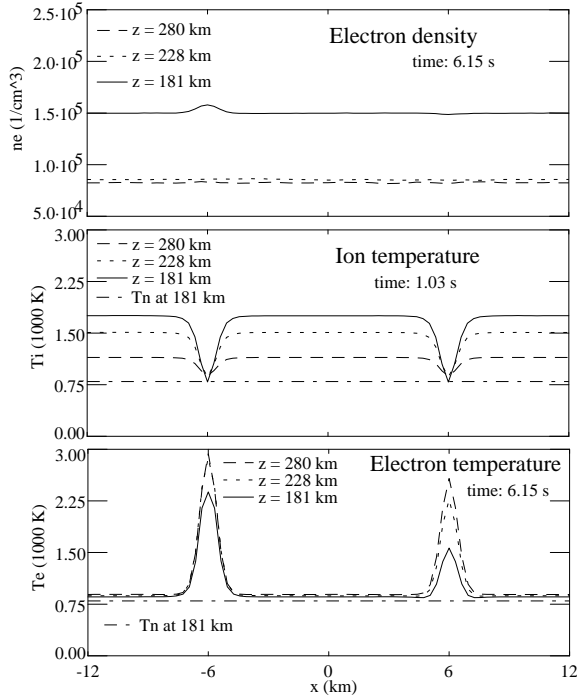


Figure 8. Profile of (top) electron density, (middle) ion temperature, and (bottom) electron temperature as a function of x for three fixed altitudes (181, 228, and 281 km). Electron density and temperature are shown for the time $t = 6.15$ s, and ion temperature is shown for $t = 1.03$ s. The plot is for the case without precipitation.

responding electron density increase, which followed a few seconds later.

Figure 8 shows the ion and electron temperatures and the electron density as functions of x for three fixed altitudes and time $t = 6.15$ for the case without particle precipitation. The electron temperature and density are plotted for time $t = 6.15$ s. To better illustrate the different electron and ion heating inside and outside the current layer, we have plotted the ion temperature for a fairly early time $t = 1.03$ when it is higher at lower altitudes. Early in the simulation, ions are strongly heated in the region outside the current layers. The maximum ion heating appears below 200 km (compare Plate 1). After 6 s the electron temperature inside both current layers ($x = \pm 6$ km) increases significantly, up to 3000 K.

Our simulation shows a number of the properties which characterize the observed event. Assuming that the field of view is first in a region outside the field-aligned current, then inside the field-aligned current, and finally in a region with enhanced electron precipitation, one would expect to

observe the following:

1. The ion temperature develops with a profile similar to that illustrated in Plate 1. Since there is no significant precipitation in this region, electron density and temperature are constant or slowly decreasing. The event presented by L99 starts with ion heating shortly after 2233:30 UT. The initially strong ion heating appears at about 170 km. The ion temperature maximum then moves to higher altitudes. The observations were acquired during solar minimum conditions. Both the altitude progression and the temporal profile of the ion temperature are similar to the ion temperature for solar minimum conditions in our simulation (bottom panel of Plate 1). During ion heating, both the electron density and temperature slowly decrease.

2. A rapid increase in electron temperature occurs when the FAC comes into the field of view. The ion temperature should decrease to the background level at the same time (Figure 8) because the fast ion flow is outside the FAC region. EISCAT data (L99) show a sudden increase of electron temperature just after the ion heating. At the beginning of the electron heating, the electron density decreases. The initial electron heating region extends from about 170 km to higher altitudes. The electron temperature increases to above 3000 K. Since the electron density is decreasing at this time, the heating is expected to be due to a source other than precipitation. Our simulation results (Plate 3) show that the electron temperature inside the current layer increases up to about 3000 K in a few seconds. The altitude extent of electron heating also agrees with the observed data, i.e., from 170 km to higher altitudes. At the time of electron heating by field-aligned current, the ion temperature decreases to the background level.

3. The electron density increases when the precipitation comes into the field of view. This is not a self-consistent result of the present 2-D fluid model but has to be assumed as a boundary condition for the incoming electron flux, similar to the 1-D transport model. Shortly after the start of the electron heating, the electron density increases, which indicates that the field of view is in a region of particle precipitation. From 2234:00 UT to about 2234:30 UT, the electron density continues to increase, with a maximum at about 130 km, which corresponds to particle precipitation with characteristic energy 1.0 keV (Figure 4). The electron temperature at the same time further increases, with the maximum slightly above 3000 K. However, the bottom edge of the electron heating region moves to higher altitude, and there is strong electron heating at altitudes above 200 km. Our simulation results of electron heating by particle precipitation (top panel of Plate 2) show reasonably good agreement. After 0234:30 UT, the electron density increases at lower altitude, with a maximum at about 125 km. This indicates that the charac-

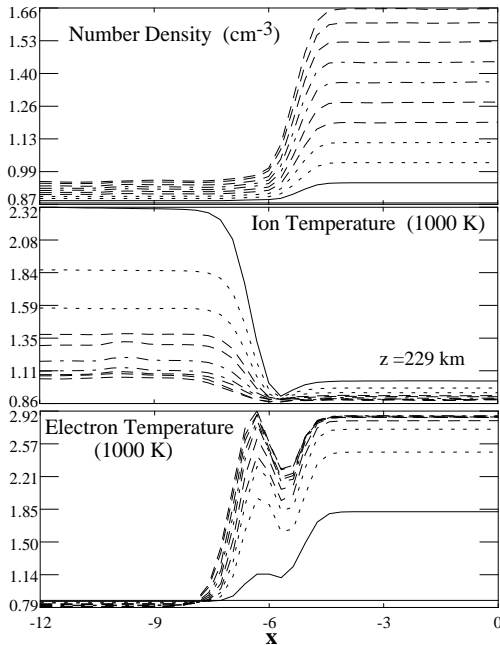


Figure 9. Profile of (top) electron density, (middle) ion temperature, and (bottom) electron temperature as a function of x for 11 different times (1 s apart) for the altitude 229 km. The case uses precipitation in the region $-5 \text{ km} \leq x \leq 5 \text{ km}$ and a modification of the Alfvén waves (see text).

teristic energy of precipitation increased to a higher value, resulting in energy deposition at lower altitudes.

Figure 9 illustrates a result where we included two additional properties compared with the results shown in Figure 8. We added an Alfvén wave with constant amplitude of half the value for the two original Alfvén wave trains to include a large-scale convection. This yields a larger convection velocity in the region $x < -6 \text{ km}$ (and $x > 6 \text{ km}$). We also included particle precipitation in the region $-5 \text{ km} \leq x \leq 5 \text{ km}$ with the same energy flux and characteristic energy as for the result of Plate 2. The result in Figure 9 shows density, ion temperature, and electron temperature in time intervals of 1 s (covering a total of 10 s) as a function of x for a constant altitude of 229 km. A scan through this structure from left to right shows the basic sequence of the EISCAT event. It should be noted, however, that there is no unique quantitative result for such a scan because this depends on how fast the scan is performed (or how fast the structure moves). Note that we also used an average over about 1 km to emulate the field of view of the radar. We did not average over time in Figure 9. The small gap in the electron temperature depends on the precise location of the precipitation region relative to the location of the field-

aligned current.

While the overall situation seems to be captured relatively well, quantitative aspects of the 2-D simulation are certainly different. In our simulation we did not attempt to introduce a time-varying ionization rate to obtain a best fit. Figure 9 illustrates that a scan through a two-dimensional fast evolving structure cannot yield a unique result. The precise distribution and time history of the Alfvénic perturbations are not known and are likely more complicated than in the simplified smooth model adopted here. However, it is shown that a strong filamentary current layer has characteristic properties in terms of convection, ion heating, and electron heating.

5. Summary and Discussion

We have reported first results from a new two-dimensional three-fluid code with application to electromagnetic coupling between the ionosphere and the magnetosphere. The simulation solves the continuity, momentum, and energy equations for neutral, ion, and electron fluid components. The ionospheric transport parameters are computed from standard formulations for the collision frequencies, and the code uses methods typically applied in one-dimensional transport computations to determine ionization, recombination, and electron cooling rates. The model includes ion inertia, such that the typical fluid plasma waves are a part of the simulation. This is particularly important for the magnetosphere-ionosphere system in which Alfvén waves are central for the interaction between the two systems. Consequently, the simulation code is well suited to describe fast temporal and small spatial changes in the ionosphere.

The two-dimensional model cannot address the deformation of FAC and discrete aurora along the auroral curtain, which requires three dimensions. However, it provides a realistic model for the formation of FAC layers by Alfvénic perturbations.

The results of this paper focus on various mechanisms of ion and electron heating. The motivation for this focus is threefold. First, it demonstrates that the code obtains reasonable quantitative results for these heating mechanisms. Second, the demonstrated heating processes depend on a temporal and spatial variation of the magnetospheric input. Finally, radar and optical observations of ion and electron temperatures and ionization in an auroral event are reproduced in many respects by the 2-D simulations.

The simulation used in this paper is complementary to the 1-D transport model used by L99. The 1-D transport model addresses the quantitative electron transport and the resulting ionization, heating, and chemistry for sufficiently energetic electrons. However, it does not and cannot address the electromagnetic changes as a result of the field-aligned

current formation. On the other side, our two-dimensional model has to include the electron transport by suitably parameterized transport coefficients.

On the basis of our results we suggest that the sequence of events reported by L99 is in part caused by the spatial structure of convection, field-aligned currents, and precipitation, in or close to the particular auroral arc structure.

For the simulation we employ boundary and initial conditions that cause Alfvén waves to propagate from the magnetosphere into the ionosphere. If the velocity and flow perturbation of the waves changes (reverses sign) across a vertical boundary, the waves carry a field-aligned current into the ionosphere.

We have demonstrated that the impact of the horizontal ion flow carried by the wave leads to fast ion heating first at lower ionospheric altitudes. The partial reflection of the wave (with a corresponding decrease in the flow velocity) and the large ion-neutral thermal contact at lower altitudes lead to a subsequent shift of the maximum ion temperature to higher altitudes. This heating does not affect the electrons. Our model predicts the correct temporal evolution on short timescales from wave reflection, ion-neutral friction, and cooling by neutrals.

The results demonstrate very significant electron heating by ohmic dissipation within a strong field-aligned current. Ohmic heating in field-aligned currents is neglected by most other models since it is of no significance on sufficiently large scales. Our model determines the current density self-consistently as a function of time for given magnetospheric boundary conditions. The horizontal ion velocity is much smaller in the current layer than outside such that ion heating is small inside the layer.

It is often assumed that discrete auroral arcs are associated with upward field-aligned current regions and corresponding Alfvénic perturbations [e.g., *Lanchester and Rees*, 1987; *Seyler*, 1988, 1990; *Otto and Birk*, 1992, 1993; *Haerendel*, 1994; *Lanchester et al.*, 1997; *Stasiewicz and Potemra*, 1998]. Thus electron precipitation should be expected in a small region within or next to the current layer. The transport model results of L99 demonstrate excellent agreement for evolution of the electron density profile, however, they also show a large discrepancy for the electron temperature without a heating source other than precipitation. Including a significant field-aligned current density can explain the rapid heating. Our results complemented by the one-dimensional transport result of L99 provide strong evidence for large field-aligned current densities in or next to discrete aurora.

Acknowledgments. The work is supported by NASA SR&T grants NAG 5–6219 and PR 201–70856 and the High Frequency

Active Auroral Research Program (HAARP), under Air Force contract F94030e-d to the University of Alaska Fairbanks. The computation is supported by the Arctic Region Supercomputer Center at the University of Alaska, Fairbanks.

Janet G. Luhman thanks W. Jeffrey Hughes and another referee for their assistance in evaluating this paper.

References

- Birk, G. T., and A. Otto, A three-dimensional plasma–neutral gas–fluid code, *J. Comput. Phys.*, *125*, 513, 1996.
- Birk, G. T., and A. Otto, Consequences of a resistive instability operating in the upper auroral ionosphere, *J. Atmos. Terr. Phys.*, *59*, 835, 1997.
- Birn, J., Computer studies of the dynamical evolution of the geomagnetic tail, *J. Geophys. Res.*, *85*, 1214, 1980.
- Borovsky, J. E., Auroral arc thicknesses as predicted by various theories, *J. Geophys. Res.*, *98*, 6101, 1993.
- Dreher, J., On the self-consistent description of dynamic magnetosphere-ionosphere coupling phenomena with a height resolved ionosphere, *J. Geophys. Res.*, *102*, 85, 1997.
- Haerendel, G., Acceleration from field-aligned potential drops, *Astrophys. J. Suppl. Ser.*, *90*, 765, 1994.
- Haerendel, G., S. Buchert, C. La Hoz, B. Raaf, and E. Rieger, On the proper motion of auroral arcs, *J. Geophys. Res.*, *98*, 6087, 1993.
- Hedin, A. E., Extension of the MSIS thermosphere model into the middle and lower atmosphere, *J. Geophys. Res.*, *96*, 1159, 1991.
- Hughes, W. J., and D. J. Southwood, The screening of micropulsation signals by the atmosphere and ionosphere, *J. Geophys. Res.*, *81*, 3234, 1976.
- Lanchester, B. S., and M. H. Rees, Field-aligned current reversals and fine structure in a dayside auroral arc, *Planet. Space Sci.*, *35*, 759, 1987.
- Lanchester, B. S., J. R. Palmer, M. H. Rees, D. Lummerzheim, K. U. Kaila, and T. Turunen, Energy flux and characteristic energy of an elemental auroral structure, *Geophys. Res. Lett.*, *21*, 2789, 1994.
- Lanchester, B. S., M. H. Rees, D. Lummerzheim, A. Otto, H. U. Frey, and K. U. Kaila, Large fluxes of auroral electrons in filaments of 100 m width, *J. Geophys. Res.*, *102*, 9741, 1997.
- Lanchester, B. S., M. H. Rees, K. J. F. Sedgemore, J. R. Palmer, H. U. Frey, and K. U. Kaila, Ionospheric response to variable electric fields in small-scale auroral structures, *Ann. Geophys.*, *16*, 1343, 1998.
- Lanchester, B. S., D. Lummerzheim, A. Otto, M. H. Rees, K. J. F. Sedgemore-Schulthess, H. Zhu, and I. W. McCrea, Ohmic heating as evidence for strong field-aligned currents in filamentary aurora, *J. Geophys. Res.*, this issue.
- Lummerzheim, D., Comparison of energy dissipation functions for high energy auroral electron and ion precipitation, Rep. UAG-R-318, Geophys. Inst., Univ. of Alaska, Fairbanks, 1992.
- Lummerzheim, D., and J. Lilensten, Electron transport and energy degradation in the ionosphere: Evaluation of the numerical solution, comparison with laboratory experiments and auroral observations, *Ann. Geophys.*, *12*, 1039, 1994.

- Maltsev, Y. P., W. B. Lyatsky, and A. M. Lyatskaya, Currents over the auroral arc, *Planet. Space Sci.*, **23**, 53, 1977.
- Maurits, S. A., and B. J. Watkins, UAF Eulerian model of the polar ionosphere, in *Solar Terrestrial Energy Program (STEP) Handbook of Ionospheric Models*, edited by R. W. Schunk, pp. 95–123, Utah State University, Logan, UT, 1996.
- Opgenoorth, H. J., I. Häggström, P. J. S. Williams, and G. O. L. Jones, Regions of strongly enhanced perpendicular electric field adjacent to auroral arcs, *J. Atmos. Terr. Phys.*, **52**, 458, 1990.
- Otto, A., and G. T. Birk, The dynamical evolution of small-scale auroral arc phenomena due to a resistive instability, *J. Geophys. Res.*, **97**, 8391, 1992.
- Otto, A., and G. T. Birk, Formation of thin auroral arcs by current striation, *Geophys. Res. Lett.*, **20**, 2833, 1993.
- Potter, D. E., *Computational Physics*, John Wiley, New York, 1973.
- Rees, M. H., *Physics and Chemistry of the Upper Atmosphere*, Cambridge Univ. Press, New York, 1989.
- Roble, R. G., The NCAR thermosphere-ionosphere-mesosphere electrodynamics general circulation model (TIME-GCM), in *Solar Terrestrial Energy Program (STEP) Handbook of Ionospheric Models*, edited by R. W. Schunk, pp. 281–288, Utah State University, Logan, UT, 1996.
- Roble, R. G., and M. H. Rees, Time-dependent studies of the aurora: Effects of particle precipitation on the dynamic morphology of ionospheric and atmospheric properties, *Planet. Space Sci.*, **25**, 991, 1977.
- Roble, R. G., E. C. Ridley, and R. E. Dickinson, On the global mean structure of the thermosphere, *J. Geophys. Res.*, **92**, 8745, 1987.
- Schunk, R. W., The terrestrial ionosphere, in *Solar-Terrestrial Physics: Principles and Theoretical Foundations*, Proceedings of the Theory Institute, Chestnut Hill, MA, pp. 609–676, D. Reidel, Dordrecht, 1983.
- Schunk, R. W., A mathematical model of the middle and high latitude ionosphere, *Pure Appl. Geophys.*, **127**, 255, 1988.
- Seyler, C. E., Nonlinear 3-D evolution of bounded kinetic Alfvén waves due to shear flow and collisionless tearing instability, *Geophys. Res. Lett.*, **15**, 756, 1988.
- Seyler, C. E., A mathematical model of the structure and evolution of small-scale discrete auroral arcs, *J. Geophys. Res.*, **95**, 17,199, 1990.
- Sojka, J. J., Global scale, physical models of the *F* region ionosphere, *Rev. Geophys.*, **27**, 371, 1989.
- Stasiewicz, K., and T. Potemra, Multiscale current structures observed by Freja, *J. Geophys. Res.*, **103**, 4315, 1998.
- Stasiewicz, K., G. Holmgren, and L. Zanetti, Density depletions and current singularities observed by Freja, *J. Geophys. Res.*, **103**, 4251, 1998.
- Wescott, E. M., H. C. Stenbaek-Nielsen, T. N. Davis, W. Murcray, H. M. Peek, and P. Bottoms, The $L = 6.6$ Oosik barium plasma injection experiment and magnetic storm of March 7, 1972, *J. Geophys. Res.*, **80**, 951, 1975.

D. Lummerzheim, A. Otto, and H. Zhu, Geophysical Institute, University of Alaska, Fairbanks, 903 Koyukuk Drive, Fairbanks, AK 99775-7320. (ao@why.gi.alaska.edu)

B. S. Lanchester and M. H. Rees, Department of Physics, University of Southampton, Highfield, Southampton SO17 1BJ, England.

Received AUGUST 13, 1999; revised FEBRUARY 10, 2000; accepted MARCH 30, 2000.

This preprint was prepared with AGU's L^AT_EX macros v5.01, with the extension package 'AGU++' by P. W. Daly, version 1.6b from 1999/08/19.